RADAR INTERFEROMETRY IN SURFACE DEFORMATION DETECTION WITH ORBITAL DATA

Interferometria de Radar na Detecção de Deformação Superficial com Dados Orbitais

Waldir Renato Paradella[1]; José Claudio Mura[2]; Fabio Furlan Gama[2] & Athos Ribeiro dos Santos[1]

[1]Instituto Nacional de Pesquisas Espaciais – INPE
Divisão de Sensoriamento Remoto – DSR
Av. Astronautas, 1758, São José dos Campos, SP, CEP: 12227-010, Brasil.
waldir@dsr.inpe.br; athos@dsr.inpe.br

[2]Instituto Nacional de Pesquisas Espaciais – INPE
Divisão de Processamento de Imagens – DPI
Av. Astronautas, 1758, São José dos Campos, SP, CEP: 12227-010, Brasil.
mura@dpi.inpe.br; fabio@dpi.inpe.br

ABSTRACT

In the last two decades, the advent of Differential Interferometric Synthetic Aperture Radar (DInSAR) technique has opened new perspectives in the use of orbital imaging radar for quantitative surface deformation measurements. In the last few years this trend was considerably expanded through the use of large stacks of SAR images collected over the same area, instead of the classical two interferometric acquisitions used in the standard configurations. Advanced DInSAR techniques are nowadays more quantitative geodetic tools rather than simple qualitative tools available for land deformation detection. The paper reviews the main SAR and INSAR concepts, the current availability of orbital SAR data, and addresses PSinSAR (Persistent Scatterer InSAR) and SBAS (Small Baseline Subset), two innovative advanced forms of DInSAR for the detection of millimetric ground displacements in various application fields. Finally, perspectives on the use of these technologies in Brazil are emphasized.

Keywords: Remote Sensing; Imaging Radar; Surface Deformation; DInSAR; PSInSAR; SBAS.

RESUMO

Nas duas últimas décadas, o advento da técnica da Interferometria Diferencial de Radar de Abertura Sintética (DInSAR) abriu novas perspectivas no uso de imagens de radar orbital para medidas quantitativas de deformação da superfície. Nos últimos anos, esta tendência foi consideravelmente expandida pelo uso de grandes conjuntos de imagens SAR coletadas sobre uma mesma área, ao invés do uso clássico de duas aquisições interferométricas usadas em configuração padrão. Técnicas DInSAR avançadas são atualmente mais ferramentas geodésicas quantitativas que simples ferramentas qualitativas disponíveis para detecção de deformação do terreno. O artigo revê os conceitos principais de SAR e InSAR, a disponibilidade atual de dados orbitais SAR e aborda as técnicas PSInSAR (Persistent Scatterer InSAR) e

SBAS (Small Baseline Subset), duas formas inovadoras de DInSAR concebidas para detecção de deslocamentos milimétricos no terreno em vários campos de aplicação. Por último, perspectivas de uso destas tecnologias no país são também enfatizadas.

Palavras chaves: Sensores Remotos; Radar Imageador; Deformação de Superfície; DInSAR; PSInSAR; SBAS.

1. INTRODUCTION

A notable advance to the detection and monitoring of ground displacements has been described with the advent of systematic data acquisition based on orbital Synthetic Aperture Radar (SAR) systems. A SAR is an active sensor (it uses its own energy source) and has day and night imaging capabilities since it uses microwaves energy. High spatial resolution images of the terrain can be obtained, and it is possible to measure the sensor to target distance by recording the time between the emission of the electromagnetic waves from the sensor's antenna towards the Earth's surface and the reception of the backscattered signal from the ground. Variations in distance measured at different times allow the detection of ground displacements. This is the basis of the Interferometric Synthetic Aperture Radar (InSAR) technique.

The first generation of Differential InSAR technology, referred as DInSAR, was proposed in the mid-90's. The potential of the technique is mainly due to: (1) the operational advantages given by the wide area coverage at low cost, (2) the high capabilities of deformation measurement, which are comparable with some classical geodetic methods, (3) the regular data acquisition over time, and (4) the availability of historical archives of SAR data. At the present time, several spaceborne SARs are in use around the world providing data for this kind of remote sensing applications.

This paper addresses the fundamentals of SAR and DInSAR, a technique based on imaging radar data to detect ground displacements with rates between a few millimeters and some centimeters per year. In addition, the paper also focuses on the Advanced DInSAR, a more recent data analysis procedure, which requires redundant observations of the same phenomenon. There are currently two broad categories of approaches that deal with multiple interferograms from a stack of SAR images: Persistent Scatterer (PSInSAR) and Small Baseline Subset (SBAS) methods. Details of these subjects and examples are given in the paper to illustrate these developments..

2. FUNDAMENTALS OF IMAGING RADAR

In the early 1900's several countries developed Plan Position Indicator (PPI) Radar for military applications. These circularly scanning devices produced a terrain format radiating in a circular way from beneath the aircraft. Since a radar is basically a device for measuring the distance of targets (radar is an acronym for radio detection and ranging), the first images of the terrain echoes were considered undesirable noise. One of the first unclassified report of nonmilitary use of radar was published by Smith in 1948 (MACDONALD, 1979). Smith's work compared PPI products with existing charts of northwestern Greenland (USA) and noted that the radar-derived data far exceeded the terrain information from available topographic maps. Imaging radar became a useful way to derive information for various application fields and opened new perspectives on the analysis and monitoring of the changes on the terrain surface as it was installed on satellites.

A SAR is a imaging radio-frequency sensor since it uses the microwave region of the electromagnetic spectrum, within the frequency interval from 0.3 GHz to 300 GHz or from 1m to 1mm, in terms of wavelength. Imaging radar satellites follow sun-synchronous orbits, and the most common orbital systems use electromagnetic waves with wavelengths in the range of X band (3cm), C band (6 cm) or L band (23 cm). The viewing geometry of a SAR is side-looking with a microwave beam radiated at an angle orthogonal to the velocity vector, i.e., the track direction of the satellite flight. A two-dimensional imaging plane (range and azimuth) is obtained with the sensor in motion and periodically transmitting pulses orthogonal to the trajectory direction (figure 1).

The combination of the motion of the satellite and the Earth makes it possible to acquire data at a common area from two almost opposite look-direction: ascending orbits with the sensor moving from South to North (East-looking) and descending orbits with the satellite moving North to South
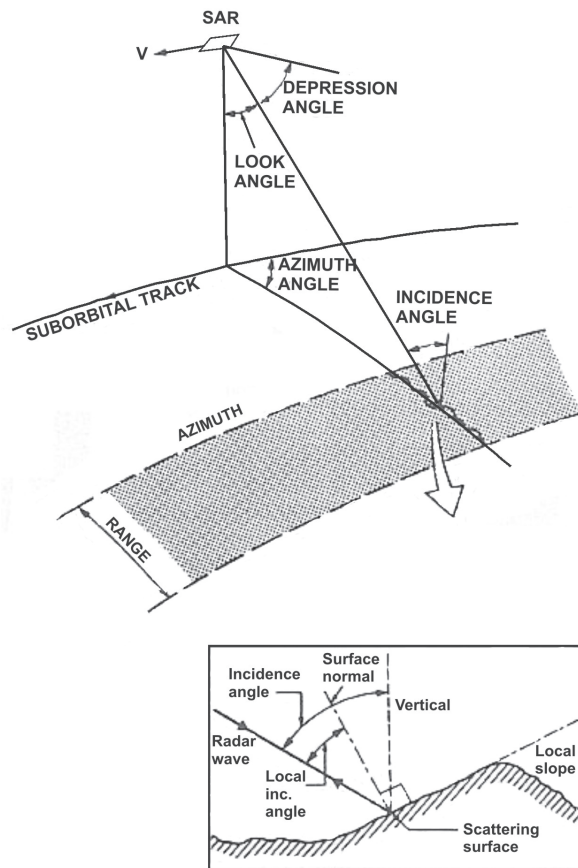
Fig. 1: SAR geometry and related angles (source: LOWMAN JR. et al., 1987).

(West-looking). This implies that targets or terrain features aligned orthogonal to the antenna are highlighted while features can be suppressed if oriented parallel to the look (azimuth) direction.

The SAR concept was originally proposed by Carl Wiley in 1951 and it is related to the idea of synthesizing a long antenna to improve the azimuth resolution as compared to real aperture radar. This author showed that a SAR platform when moving will generate a Doppler shift leading to an azimuth frequency spread when passing over a target. Echoes reflected from targets in front of the moving sensor are frequency shifted relative to the echoes reflected from behind (WILEY, 1954).

A generic SAR is composed of the acquisition system, which makes the radar measurements, and a processor (Doppler) that converts the backscattered signal into an image. The SAR focusing principle involves transmitting a linear frequency modulated (FM) chirped pulse, allowing the use of longer pulses to increase the pulse energy. Basically, a SAR (1) transmits pulses from the antenna to the terrain, (2) receives pulse responses in range and focuses them defining the spatial

resolution (range), (3) accumulates overlapping time histories of the backscattered signal at each range samples from a sequence of transmitted coherent pulses, (4) uses the phase history of the sample sets at each range to focus the signal returns along the azimuth direction into resolution cells, (5) measures the distance (range) from the SAR to each sample point on the ground, and (6) measures the signal attributes of amplitude and phase of the received signal (LIVINGSTONE et al., 1999).

The SAR measurement cell is described by two-dimensional spatial resolutions: azimuth (along-track direction) and range (across-track direction) resolutions. The azimuth resolution can be achieved in two ways leading to the same result: synthetic array or Doppler synthesis approaches (WERLE, 1988). For the synthetic array, the finest possible azimuth resolution for a point target corresponds to $l/2$ where l is the antenna length (MOORE et al., 1975). The same value is obtained considering the azimuth impulse response function of the sensor defined by the azimuth bandwidth and the azimuth focusing signal processing (Doppler synthesis). The range resolution is related to the pulse bandwidth of the transmitted radar signal and it is achieved by measuring the relative time delays of each echo component from a transmitted pulse. Thus, it is possible to obtain imagery at high spatial resolution over great distances.

It is important to mention that a SAR detects backscattered energy from a resolution cell that is three-dimensional in the illuminated space, described by the range and azimuth observations and the height limited by the vertical illumination pattern of the antenna (RANEY, 1988). The illumination is characterized by transmitted monochromatic pulses, with structured phase fronts that can be represented by spherical surfaces centered at the sensor. When the radiated electric field interacts with a target, it will induce surface charges on the object and electric currents within it. The characteristics of this interaction are controlled by the wave polarization, the complex dielectric constant, the target shape and orientation. Within the resolution cell, each scatterer, that is illuminated by the transmitted waves or by the combination with forward scattered waves (multiple scattering), will produce waves with components travelling in all directions. All the individual scatterer will contribute to the

backscattered signal through vector addition (LIVINGSTONE et al., 1999).

Using processing techniques, the intensity and phase of the backscattered signal of each ground resolution cell can be calculated in the form of a complex-valued image. Thus, a SAR image is represented by an array of digital numbers (pixels) expressing a matrix of complex numbers defined by amplitude and phase values. It is important to mention that spatial resolution and pixel are distinct concepts. A pixel corresponds to the location of a digital sample, and not to an area in the scene. According to the Nyquist theorem, the transformation of the signal responses to the digital domain implies that there should be at least four pixels for each resolution cell. Finally, since a SAR is a phase-coherent system, an interference called speckle is common, appearing as a noise-like modulation in the image intensity and as a phase noise in the complex data (RANEY, 1988).

The amplitude or intensity of the SAR image is determined primarily by the target geometric (surface roughness, slope, shape) and its electric (complex dielectric constant) characteristics, whereas the phase of the SAR image is determined primarily by the distance between the antenna and the targets. If targets present responses that change during the observation intervals, then the relative phase of the backscattered responses will change and this detection is the basis for radar interferometry. Finally, it is relevant to mention that microwaves are able to travel through the atmosphere without relevant signal loss, providing all-weather and day-night capabilities. These two attributes are fundamental for mapping cloudy environments and monitoring ground displacement phenomena, where systematic scene acquisition is necessary.

3. INTEROMETRIC SAR (InSAR)

The phase of a resolution cell, represented by the argument of a complex number, is the phase resulting of the contribution of many scatterer mechanisms within the resolution cell. The phase can be rotated due to reflection, depending on the dielectric properties of the scatterers, or be delayed depending on the relative position of the scatterers within the resolution cell. The phase of the received signal is uniformly distributed between 0 and 360 degrees or 0 and 2π radians (figure 2). The phase sensitivity to a distance variation is high: a phase shift

of 2π corresponds to $\lambda/2$ (λ is the sensor wavelength). The distance from the sensor to the ground target is measured along the Line of Sight (LOS) or slant range dimension (R), the phase introduced by this distance is given by:

$$\Phi = (2\pi/\lambda)2R \qquad (Eq.1)$$

Since it is not possible to separate the different phase contributions, the phase values of a single SAR image are of no practical use. A more suitable approach is the analysis of phase difference between two or more SAR images. An interferogram or InSAR image is thus created by combining radar signals from two spatially or temporally separated antennas after proper image registration on a pixel-by-pixel basis. Two situations are possible: two antennas on the same platform acquiring simultaneous scenes or one antenna acquiring images in almost identical viewing geometry at two distinct times.
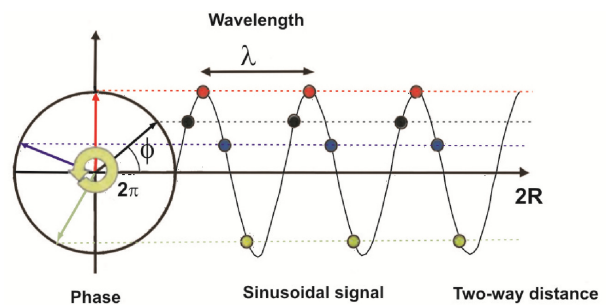

Fig. 2: A sinusoidal function (sin Φ) is periodic with a 2π radian period and expressing a linear dependence of the phase Φ on the slant range distance R (source: ESA, 2007).
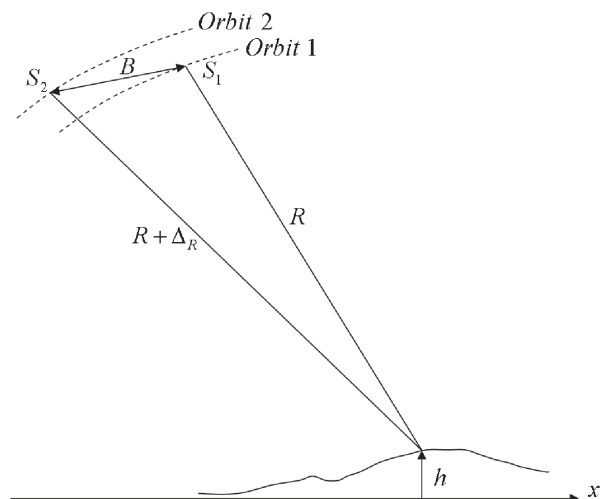

Fig. 3: Repeat-pass InSAR geometry.

The second case is known as repeat-pass InSAR, depicted on the figure 3, where B is the baseline (representing the distance between the acquisitions S1 and S2), ΔR is the slant range difference and h is the terrain height.

The interferometric phase difference for the InSAR geometry shown in the figure 3 is represented by:

$$\Delta\Phi = (4\pi/\lambda)\,\Delta R \qquad \text{(Eq. 2)}$$

From figure 3 and equation (2) we notice that a variation in height h causes a variation in ΔR and consequently a variation in $\Delta\Phi$, which is the basic idea to measure the topographic height with SAR interferometry. An example using the same platform with two antennas was the Shuttle Radar Topography Mission (SRTM) with the goal of producing digital elevation models.

The measured interferometric phase is composed by various components such as (a) topography height, (b) uncertainty in orbital determination, (c) atmospheric delays, (d) system noise and (e) processing strategy (Massonnet and Feigl, 1998). The interferometric phase can be measured from the complex-valued resolution element only in module 2π (represented by fringes or concentric bands of colors). The total range difference between the two observation points that the phase represents (figure 3) in general can be many multiples of the radar wavelength or, expressed in terms of phase, many multiples of 2π. The typical approach for determining the unique phase that is directly proportional to the range difference is to determine the relative phase between pixels via the so-called "phase-unwrapping" process. (ROSEN et al., 2000). Considering that two SAR images are acquired simultaneously (i.e., single-pass InSAR), in a area with a deformation or not, these InSAR images can be only used to derive a DEM (Lu et al., 2007). However, if two images are acquired of the same area from the exact same position, at different time, the phase difference is related to the topography but can also be related to ground surface movements toward or away along the satellite LOS during the two acquisitions. Since it is almost impossible to acquire two scenes of a common area using the same viewing geometry and at distinct times, a set of three images is generally used to detect surface changes. The topographic effects are determined using a first interferogram produced from a pair taken during a short interval. This topographic contribution will be removed from a second interferogram created from two scenes acquired during a longer time interval. The final product will contain fringes due to surface deformation. Each fringe represents one-half wavelength of surface movement. In the case of the ERS satellites, this is less than 3 cm (DEHLS, 2006).

In summary, spaceborne InSAR has shown a remarkable potential for two particular applications: (1) the production of high resolution DEMs with pairs acquired from slightly different viewing geometry, and (2) the detection of surface deformation (DInSAR) from pairs spanning a convenient time interval. Examples of both applications can be seen in GRAHAM (1974) and ZEBKER and GOLDSTEIN (1986). However, conventional InSAR has not yet become a fully operational tool with limitations caused by temporal and geometrical decorrelation and to atmospheric effects. Temporal decorrelation makes interferometric measurements unreliable due to changes in the relative scatterer positions within the resolution cell (ZEBKER and VILLASENOR, 1992). The use of short revisiting times can partially limit the effect, but only if the purpose is the DEM production. Reflectivity variations as a function of the incidence angle (geometrical decorrelation) also limit the number of image pairs for applications, unless this phenomenon is reduced due to the point-wise character of the target which will be discussed further with Advanced DInSAR techniques.

4. DIFFERENTIAL INTERFEROMETRY (DInSAR)

DInSAR is based on the computation on a pixel-by-pixel basis of the difference of phase between two images acquired at distinct times. The first demonstration of the repeat-pass DInSAR to detect ground displacements was presented by GABRIEL et al. (1989). The phase value of a SAR image can be expressed by the following equation (PIGORINI et al, 2010):

$$\Phi = \Psi + (4\pi/\lambda)r + \alpha + n \qquad \text{(Eq.3)}$$

where Ψ is the phase reflectivity, r is the sensor to target distance (slant range), α is the atmosphere contribution, and n is a sensor noise term. Assuming that target reflectivity and atmosphere terms are

constant under two acquisitions, and the system noise is negligible, the phase values from an interferogram will be proportional to the displacement between the two acquisitions. Thus, any target displacement along the satellite LOS creates a phase shift in the signal that can be detected by comparing the phase values acquired at different times (figure 4).

The repeated acquisition of images over a given area is usually performed by using the same sensor, or sensors with identical system characteristics, as it was the case of ERS-1 and ERS-2, and presently with the COSMO-Skymed constellation (REALE et al., 2011). With the advent of the ERS-1 in the 1990's several results were presented including the study of surface displacement due to glacier dynamics (GOLDSTEIN et al., 1993), volcano deformation (MASSONNET et al., 1995; AMELUNG et al., 2000), and earthquakes (MASSONNET et al., 1993; MASSONNET and FEIGL, 1998). Archive of data acquisition is available back to 1992, and currently distinct systems are operational for applications (table 1).

It is important to mention that different factors reduce the quality of DInSAR results. The most important is related to temporal-decorrelation phenomena caused by the variation of the electromagnetic properties of the radar targets. If the phase reflectivity value of a certain image pixel changes with time, the generation of an interferogram cannot highlight the displacement values, since the first term in the equation (Eq. 1) cannot be considered identical in the two SAR images. The impact of temporal decorrelation phenomena increases as the temporal baseline of the interferogram (i.e. the time lag between the two SAR acquisitions) increases. Of course, different targets are characterized by different decorrelation times: areas covered by vegetation change reflectivity much more quickly than rocky or urban areas. Apart from phase decorrelation, propagation effects in both troposphere and ionosphere can differ significantly during the first and the second acquisition, thus creating phase disturbances hindering the interpretation of the interferogram. An example of a DInSAR application with ENVISAT ASAR can be seen in figure 5.

Considering that in the most case the coherence spatially is low due to the temporal decorrelation, caused by changes in target responses, the DInSAR presents limitations when
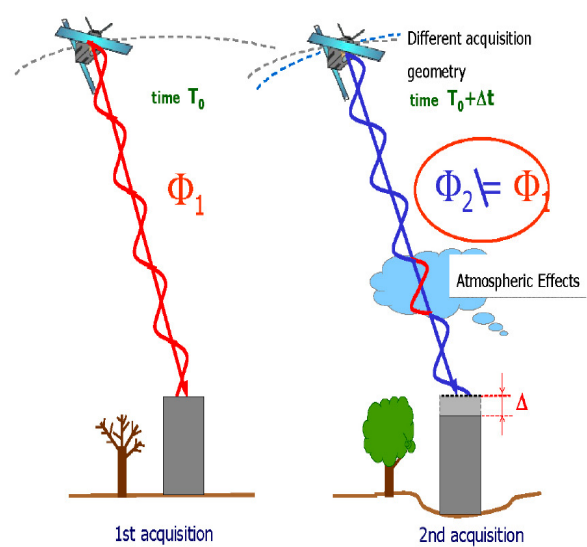

Fig. 4: Differential surface movements will result in a different measured phase using a SAR system with two acquisitions at different times and under same acquisition geometry (Source: DEHLS, 2006).
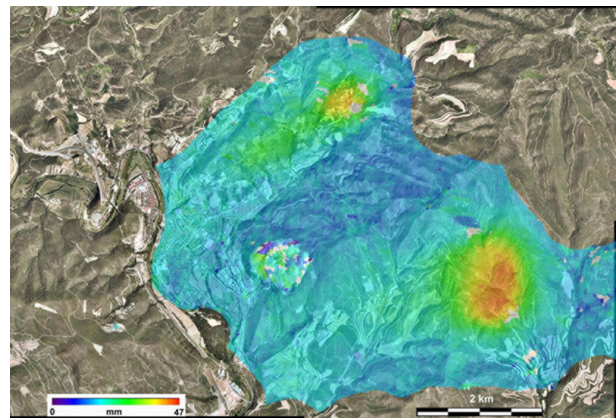

Fig. 5: Deformation map over Solsona mining (Catalunya, Spain). The blue-red scale increases subsidence. The map has been produced from a single ASAR differential interferogram with temporal baseline of 35 days. (courtesy: Institut de Geomàtica, Spain).

applied to vegetated and urban areas. The alternative of using DInSAR techniques based on the data processing from multiple acquisitions to form time-series of deformation overcomes this limitation, with a reduction of uncertainty contributions that are common in single interferograms. There are currently two broad categories of methods that use multiple images: Persistent Scatterer Interferometry (PSI) and Small Baseline Subset (SBAS). The term PSI is related to InSAR techniques that analyze the temporal phase evolution of individual coherent point scatterers. It was proposed by FERRETTI et al.

Table 1 – Orbital systems with capability of DInSAR applications

Satellite	Property	Revisiting time (days)	Resolution (range x azimuth)	Band	Polarization	Operation
ERS-1/AMI	ESA	35	30 x 26 m	C	VV	1992 - 2001
ERS-2/AMI	ESA				VV	1995 - 2011
RADARSAT-1	CSA	24	Up to 10 x 8 m	C	HH	1995 up to now
ENVISAT/ASAR	ESA	35	30 x 26 m	C	Single: HH, VV; Dual: VV/HH, HV/HH, VH/VV	2002 up to now
ALOS/PALSAR	JAXA	46	9.6 x 4.49 m	L	Single: HH, VV; Dual: HH/HV, VV/VH; Quad.: HH/HV/VH/VV.	2006 - 2011
TerraSAR-X	GSA	11	Up to 1 x 1 m	X	Single: HH or VV; Dual: HH/VV, HH/HV, VV/HV.	2007 up to now
COSMO-SkyMed	ISA	16		X	Single: HH,HV,VH,VV; Dual: HH/VV, HH/HV, VV/VH.	2007 up to now
RADARSAT-2	CSA	24		C	Single: HH,HV,VH,VV; Dual: HH/HV, VV/VH; Quad.: HH/HV/VH/VV.	2007 up to now

CSA - Canadian Space Agency; ESA - European Space Agency; GSA - German Space Agency;

ISA - Italian Space Agency; JAXA - Japan Aerospace Exploration Agency.

(1999) and deals with privileged phase coherent radar targets within a resolution cell that present stable amplitude and phase, throughout all of the images within a data stack. Targets that work as PS are stable radar reflectors and can be man-made structures (street lights, transmission towers, buildings, bridges, exposed pipelines, roof structures, objects that are associated to dihedral, trihedral responses) or natural targets (rock outcrops, un-vegetated ground surfaces, boulders, etc.). In images where most pixels contain multiple scatterers of similar strength, the PSI approach is less optimal since the backscattering responses of these pixels vary substantially with look angle. In this case, an approach that interfere only pairs of images for which the difference in look angle is small is preferable. This is the basis of the Small Baseline Subset approach (BERARDINO et al., 2002), which relies on an appropriate combination of differential interferograms created by using SAR image pairs characterized by a small orbital separation (baseline) with reduction of the spatial decorrelation phenomena. Both methods are discussed with more detail and with examples.

4.1 Persistent Scatter (PSInSAR)

PSI technique uses large stacks of images to generate differential interferograms with respect to one common master , normally selected in the center of the time series to improve the coherence to the set of differential interferogram. Figure 6 shows a configuration example for three normal baselines Bn in relation to the master track (S_M) and $\Delta\phi_{Mi}$ is the interferometric phase diference (interferogram) of the acquisition "i" in relation to the master track.

All combinations of baselines are employed, even those exceeding the critical baseline. The PSI approach (FERRETTI et al., 1999, 2000, 2001) relies on identifying pixels whose scattering properties vary little with time and look angle (coherent pixels namely persistent scatterers). Pixels that are dominated by a singular scatterer best meet these criteria; therefore, images are processed at full resolution to both increase the chance of there being only one dominant scatterer present, and to reduce the contribution from other scatterers within each pixel. In images where most pixels contain multiple scatterers of similar strength, even at the highest possible resolution, the Persistent Scatterer
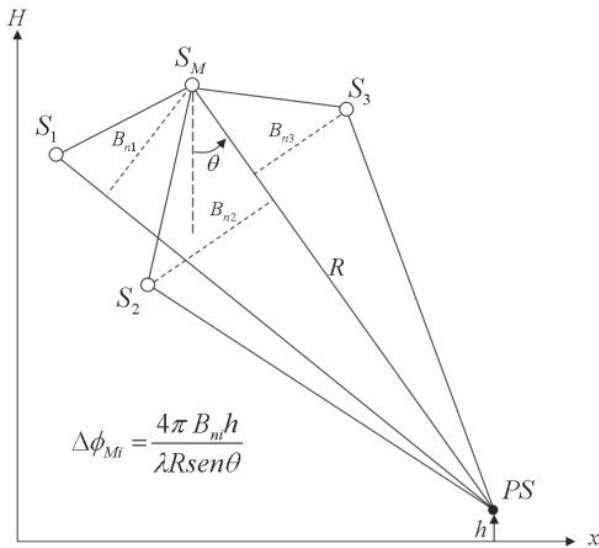
Fig. 6: Baseline configuration for four acquisitions.

Fig. 7: Temporal sampling of a deformation phenomena performed with DInSAR and PInSAR techniques (source: CROSSETTO et al., 2005).

approach is less optimal, as the scattering characteristics of these pixels vary substantially with look angle.

The PinSAR technique is limited by the number of available SAR images temporally distributed (temporal sampling), to be able to detect the desirable deformation in time. Figure 7 shows an example of what can be measured with a certain number of SAR acquisitions. It is noted that with only two acquisitions, M and S, the DInSAR technique can be applied enabling the measurement of only the deformation D(ts) – D(tm). By using N acquisitions, the PSInSAR technique can be applied enabling the measurement of the entire deformation, except on the interval of S5 an S6, for lack of images, characterized by an under sampling interval. The temporal sampling and the number of aqusitions play a very important role to detect deformation phenomena in time.

The measured differential phase ϕ_{dpha} is composed by contributions from the uncompensated topography ϕ_{topo}, of the deformation (which we want to know) ϕ_{defo}, of the atmosphere phase delay ϕ_{atm}, of the orbit error ϕ_{orb} and the noise ϕ_{noise} The measured differential phase can be written as (ADAM ET AL 2004):

$$\phi_{dpha} = \phi_{topo} + \phi_{defo} + \phi_{atm} + \phi_{orb} + \phi_{noise} \quad (Eq.\ 4)$$

From the equation 4 we notice that the measured phase ϕ_{dpha} is contaminated with many unknown phase components. The goal is to separate the movement phase component ϕ_{defo} from the others. To deal with this problem, the PInSAR
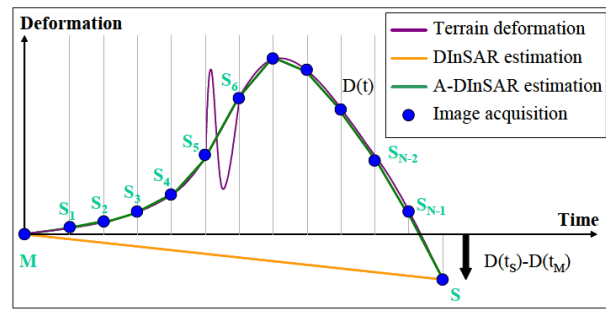
techniques make use of suitable data modeling and analysis procedures, that associated with appropriated statistical treatments of the available measured observation, make the estimation of different parameters possible.

The modeling strategies are strictly dependent on the type of application at hand. Anyways, the ability to fully describe a deformation phenomenon depends on the number of available images, and spatially on the availability of pixels which are characterized by low level of phase noise (ϕ_{noise}). In addition, the PInSAR techniques usually present, the advantage of a high data redundancy, which allows quantitative results to be achieved, both in terms of precision and reliability (CROSSETTO et al. , 2005).

By proper modeling of the phase component due to the terrain movement ϕ_{defo}, it is possible to estimate the spatial and temporal evolution of the deformation. Often the temporal evolution of the deformation is modeled with linear functions (FERRETTI et al., 2000; FERRETTI et al., 2001). CROSSETTO et al. (2005) modeled the deformation by stepwise linear functions, whose parameters are computed by least squares adjustment. Other approaches which allow a more complex description of the temporal behavior of the deformation can be found in BERARDINO et al. (2002), MORA et al. (2002), COLESANTI et al. (2003), LANARI et al. (2004) and WEGMULLER et al. (2010).

The residual topographic error ϕ_{topo} is given by the difference between the true height of the scattering phase center of a given pixel, and the height given by the employed DEM. The estimation of this phase contribution is based on the diversity of the perpendicular baseline (Bn) in the stack of the images used. The topographic phase error component for

each interferogram is a function of the perpendicular baseline (FERRETTI et al., 2000). Therefore, given a set of interferogram, the wider the spectrum of Bn, the better the configuration to estimate ϕ_{topo}. This phase component plays an important role not only for modeling purposes but also for geocoding purpose. By using the estimated residual topographic error the topographic error can be largely reduced, thus achieving a more precise geocoding (CROSSETTO et al., 2005). Using large baselines, which range in the interval of ± 1200 m, COLESANTI et al. (2003) achieved a standard deviation of the estimated ϕ_{topo} less than 1 m.

The atmosphere phase contribution ϕ_{atm} of each image of the used SAR stack, called Atmospheric Phase Screen (APS), can be estimated, starting from the phase component of the interferograms derived by combining pair wise the SAR images. The strategies used to estimate the APS contributions usually exploit the spatio-temporal correlation characteristics of the APSs, i.e., that the atmospheric effects are usually uncorrelated in time, while they are spatially smooth (FERRETTI et al., 2000). The accuracy of the estimation of the atmospheric phase contributions relative to the master image depends on the number of available images. In fact, only if APS contributions are properly estimated and removed it is possible to avoid the strong degradation of the PS phase quality caused by the atmospheric effects.

The inaccuracies in the orbit data cause systematic phase errors ϕ_{orb} in interferograms. The reason is that the computed reference phase, the so-called flat-earth phase, which is subtracted from the interferogram, is incorrect. Since the reference phase is mainly a function of range, the orbit errors manifest mainly in range direction. The orbit error phase is assumed to be small for most interferograms. HANSEN (2001) has shown that the maximum number of residual orbit fringes is less than one (95% confidence interval) in a 100x100 Km^2 if 5 cm radial and 10 cm across-track rms is assumed for the orbit precision. Since normally, precise orbits estimated by the GFZ (GeoForschungsZentrum) are used, in general the residual reference phase caused by orbit errors is smaller than a few radians over the area of interest. The residual orbit trends are assumed to be uncorrelated between acquisitions, and their impact on the estimated displacement field is thus assumed to be small (KAMPES, 2006).

The noise phase term in the equation 04 (ϕ_{noise}) is caused, among others, by thermal noise, quantization of the signal in the D/A converter, approximations made during the processing to generate de images, corregistration errors, temporal decorrelation and baseline decorrelation. Only pixels characterized by low level of phase noise are exploited to derive the deformation. This requires adopting a pixel selection criterion. The standard PinSAR technique uses the coherence-bases pixel selection (BERARDINO et al., 2002; MORA et al., 2003; LANARI et al, 2004; CROSSETTO et al, 2005). Another important class of PinSAR technique uses as a pixel selection criterion the stability of the SAR amplitude (FERRETTI et al., 2000; WEGMULLER et al., 2010)

Nowadays most of the software package that perform the PinSAR technique can work with both the coherence or amplitude base selection criteria. The choice of the selection criterion depends on the application at hand. The coherence-based methods work well over long-term coherent areas, like urban, suburban and industrial areas. The coherence of a given pixel is estimated over a window centered on the same pixel; if a single and very coherent target is located in a very noisy area it will have an estimated low coherence value. This does not occur with if it is used an amplitude criterion, which works at full resolution and which select the pixel without considering the neighborhood pixels (CROSSETTO et al., 2005).

Currently in the PSInSAR research, an important goal is to provide deformation observations characterized by high quality in terms of accuracy, precision and reliability, which are comparable with those of the observations coming from the geodetic techniques. This goal can only be achieved using a high observation redundancy, and by implementing appropriate data analysis tools. Another topic that is receiving particular attention is the validation of the PSInSAR products, which is difficult, especially for the extension of the measured areas where often there are no reference data available. Another complication comes from the relatively high quality of the PSInSAR and the consequent difficulty to get suitable reference data of higher quality (CROSSETTO et al., 2005).

A new algorithm known as SqueeSAR was recently presented (FERRETTI et al., 2011) to deal with persistent scatterers (PS) together with distributed scatterers (DS), aiming at overcome the limits of PSInSAR technique. This new technique takes into account the different statistical behavior for PS and DS, and can be jointly processed without the need for significant changes to the traditional PSInSAR processing chain. The accuracy of PS ground displacement measurements lies in the millimeter range, for linear deformation even higher than 0.1 millimeter per year. It is important to mention that in monitoring the stability of an individual target, such as a building, the high repeat rate of new acquisitions leads to a timely identification of changing deformation characteristics. The potential of this latest technology can be highlighted with two examples of deformation maps based on the SqueeSAR algorithm (figures 8 an 9).

During the last two decade a big amount of data has been collected with SAR sensors in C and X bands (ERS1/2, RADARSAT 1/2, ENVISAT ASAR, TerraSAR-X, Cosmo-Skymed) enabling the development of the DInSAR and PSInSAR techniques. With L band, some examples with DInSAR technique are found in HASHIMOTO et al. (2009), CHINI et al. (2010) and MIYAGI et al. (2009) using ALOS/PALSAR data. A PSInSAR example with L band is found in DAITO et al. (2003) using JERS-1 data. In this study, the authors pointed out that the use of L band data can bring some advantage in terms of the coherence improvement, due to the capability of L band to penetrate in vegetated areas, yielding more points selectable as PS, even if the precision of the single measurement with L band may be low, since it scales with the wavelength, but the statistics of using more points can increase the precision. Daito et al. (2003) remarked that as the L band wavelength is bigger than X and C band, the first can be more robust to measured motion with higher velocity, as expected in land sliding areas, being less susceptive to aliasing effect when compared to X and C band.

4.2. Small Baseline Subset (SBAS)

The technique SBAS (Small Baseline Subset) is an DinSAR algorithm that employs least squares technique to detect the deformation of the Earth's surface and analyze its temporal evolution, generating deformation maps and average speed of time series.

BERARDINO et al. (2002) proposed this technique in which a combination of multiple sets of SAR interferograms generated by a proper selection of SAR data pairs was used to provide a dense map of deformation. These pairs were characterized by a small spatial and temporal separation (baseline) between the orbits of the acquisition, increasing the temporal sampling by using all acquisitions from different subsets of small baseline and preserving the system's ability.

SBAS technique allows generating maps of average deformation and follows the temporal displacement evolution of individual image points, which can be done in two spatial scales: medium resolution (ground resolution of about 100 x 100 m) and full resolution (resolution ground of approximately 10 x 10m, LANARI et al., 2004). SBAS technique in full spatial resolution has also been widely applied in detailed studies of the deformation of man-made structures such as buildings, reservoirs, power plants etc. The key point of SBAS technique, besides interferograms multilook use, is the choice of the input SAR pairs involved in the interferogram generation in order to minimize the spatial baseline, thus reducing the decorrelation phenomenon and topographic errors.

The interferograms generated in this process form a redundant network that interconnects the images within a baseline time and space. The first step of the procedure requires the evaluation of low-pass filtering (LP) in the range direction of the differential phase, which may include large-scale spatial patterns of deformation, topographic errors caused by failure in the digital elevation model used, and possible contributions caused by atmospheric heterogeneities between acquisitions (often referred to as atmospheric phase artifacts). After subtracting the low spatial frequency components, the patterns of residual phase obtained from the interferograms among the temporal data are related to the deformation of high-frequency surface. These features allow minimizing some effects (such as spatial and temporal noise decorrelation) that disturb the data, increasing the number of points per unit area where the goal is to provide reliable deformation measurements.

The products obtained by this method are therefore characterized by a high density of spatially monitored points, which have an accuracy of about 1 mm / year in measures of average deformation

© 2011 Tele-Rilevamento Europa
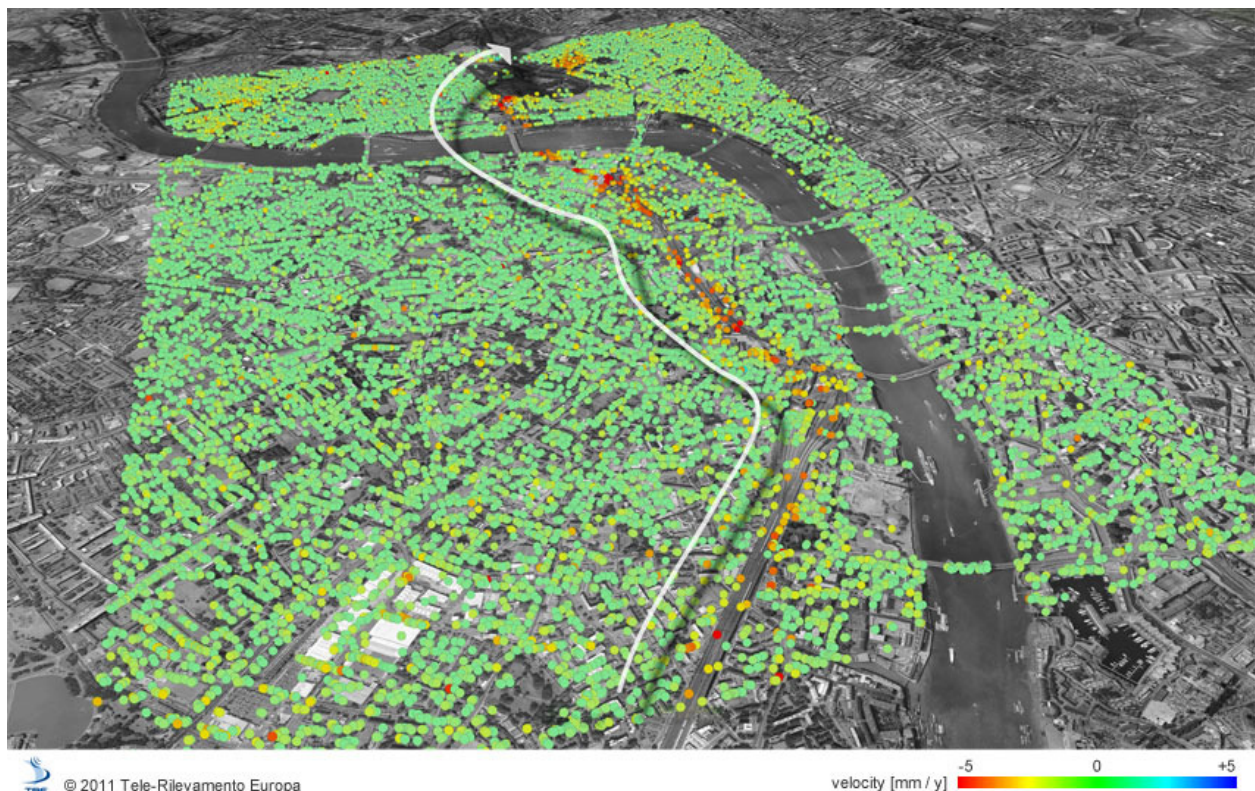
velocity [mm / y]   -5   0   +5

Fig. 8: Surface deformation effects due to tunneling of the Jubilee underground line, London. Construction of the tunnel took place during the 90's and was completed in 1999. Period of SqueeSAR™ analysis with ERS data covers the construction phase from May 1992 up to Dec 2000. Background image: Google Earth (courtesy: TRE).

speed, and about 5 mm on the measures of deformation (CASU et al., 2006). Moreover, the typical size of the analyzable area (average spatial resolution) is approximately 100 x 100 km, although the applicability of the technique has also been demonstrated to much larger areas. An extended version of SBAS algorithm is actually able to generate maps of speed and time series of deformation over large areas (spatial extent of the order of tens of thousands of km^2) and to provide information on the characteristics of space-time deformation accurately identified.

An evolution of the technique described above, especially important for the continuity in the monitoring of surface deformation, is the possibility to use data acquired from different sensors, since they are characterized by the same illumination geometry. PEPE et al. (2005) developed an algorithm that offers the advantage of being able to extend the series with the use of sensor data acquired by ERS-1 and ERS-2, launched in 1991 and 1995. This processing is able to join the data acquired by ENVISAT sensor (in orbit since 2002) as well as, to increase a deformation analysis of higher time intervals.

The current state of SBAS procedures available allows obtaining maps and deformation time series corresponding around 30 days using ERS-1/2 and ENVISAT data set. This technique was successfully applied in analyzing the deformation in prone areas as volcanic, seismic, anthropogenic etc. Some examples of the application are the monitoring of Mount Etna, Vesuvius, Teide Peak (FERNANDEZ et al, 2009.), Campi Flegrei (TRASATTI et al, 2008.) and Long Valley. In such contexts large deformations usually characterized by non-linear trends have often been identified. An example of deformation measurement using SBAS in Lisa Peninsula (Death Sea) is presented in Figure 10 .

In general, with SBAS technique it is possible to better monitor non-linear displacements, where acceleration phenomena can be an indication of high risks of collapses (landslides, sink-holes etc.). SBAS approach is more robust to these effects when compared with PS technique, showing higher density and more complete deformation patterns, still of great interest even if increasing the correlation of the measurements among adjacent pixels. The robustness of SBAS is also confirmed when the time
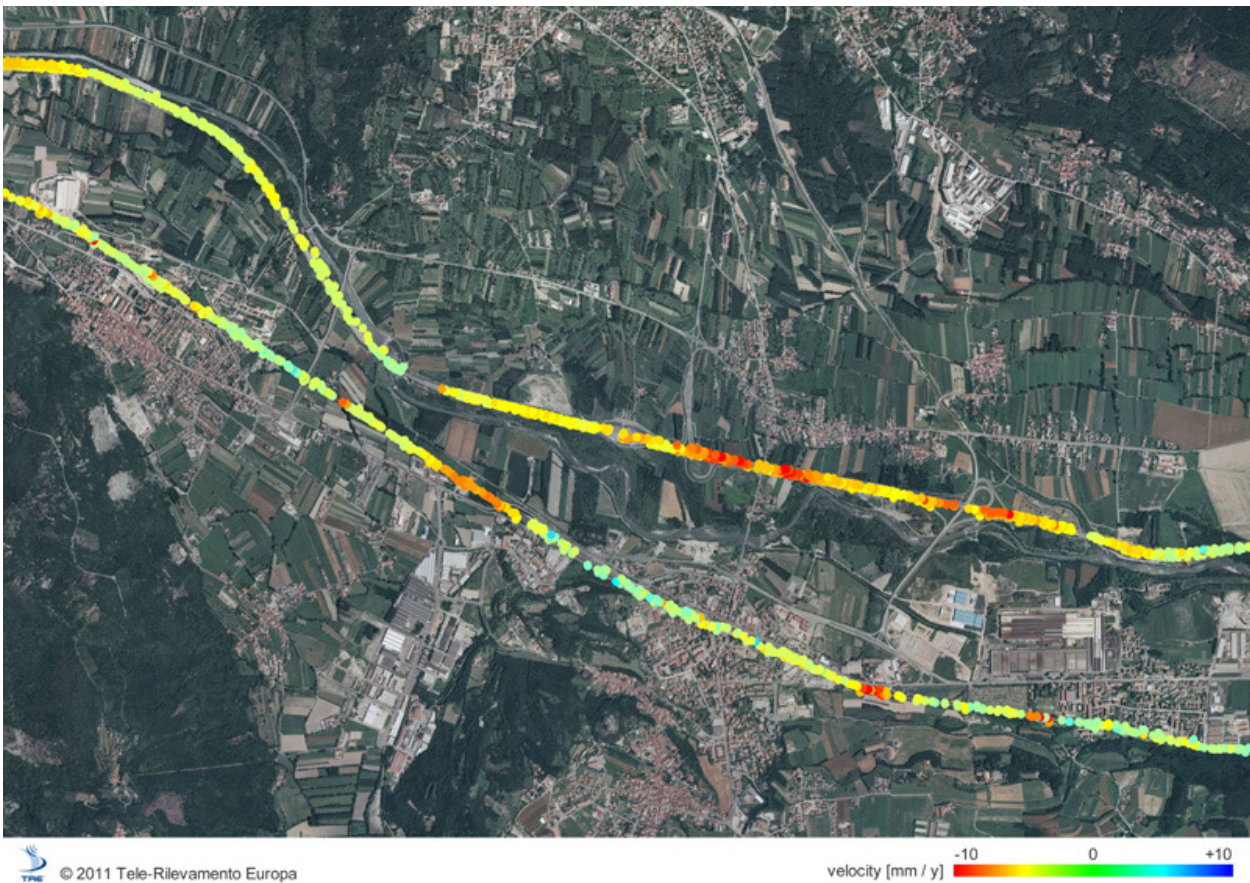
Fig. 9: SqueeSAR™ deformation map produced from a RADARSAT-1 dataset (Apr 2003 - Dec 2009) along a motorway (top) and a railway (bottom), Italy. A displacement time series is provided with each measurement point, allowing the identification of areas of differential movement along linear infrastructure. Only ground measurement points identified along the road infrastructure are shown. Background image: Google Earth (courtesy: TRE).
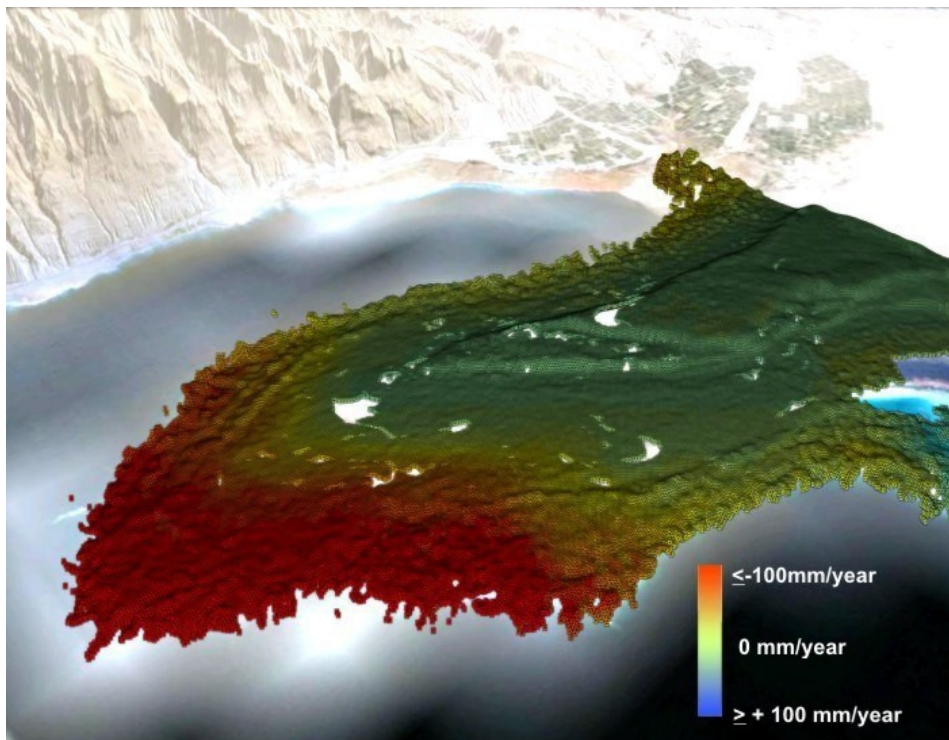

Fig. 10: Deformation map using SBAS approach in Lisa Peninsula (Death Sea) based on 42 ENVISAT ASAR scenes, from 2002 until 2010 (courtesy: SARMAP company, Purasca/Switzerland).

series is down-sampled, still providing acceptable results when exploiting 8 images only, instead of the minimum of 20 required by PS analysis.

5. CONCLUSIONS

High precision monitoring of surface deformation phenomena with DInSAR has evolved from the interpretation of a few InSAR image pairs to the analysis of time-series InSAR images. The main goal of the time-series analysis has been to reduce artifacts caused by several factors (atmospheric delay anomalies, orbit errors, loss of coherence measurements) in order to improve the accuracy of deformation measurement and monitoring. Advanced DInSAR techniques such as PSinSAR and SBAS were proposed to overcome the drawbacks of conventional DInSAR analysis and are powerful innovative tools for monitoring of surface deformation phenomena with a precision of centimeter or sub-centimeter for C-band sensors, and a few centimeters for L-band sensors. They expand the applicability of SAR interferometry from large, regional-scale to local-scale application without requirements of ancillary in situ instruments. The possibility of dealing with large amount of data in a limited amount of time makes these SAR techniques interesting tools in a wide range of application fields, providing a high density of ground measurement points for the quantitative measurement of both historical and ongoing surface movement. The wide range of applications encompasses the regular update of ground deformation related to engineering geology projects or overall instability analysis linked to settlements and/or deterioration of engineering structures. The main applications are related to Transport (roads, railways, tunneling activities, bridges, pipelines), Mining (slope stability monitoring in open pit and underground) and Oil/ Gas reservoirs, Natural Hazards (landslides, ground instabilities), Energy (power plants, dams and reservoirs) and Urbanism (single building, ground water extraction, flood defences, legal disputes). With the planned new SAR missions (ex: RADARSAT Constellation Mission), it is reasonable to assume that in the near future there will be systems providing almost daily data acquisition, which will expand dramatically the DInSAR capabilities to land surface detection and monitoring. Taking into account that the Brazilian economy has been growing consistently over the past few years, and

has become one of the major economies of the world, and the Brazilian government has recently launched a special program for economic development acceleration, the perspectives of the use of these technologies are extremely favorable.

ACKNOWLEDGEMENTS

REFERENCES

ADAM, N.; KAMPES, B.; RINEDER, M. 2004. *Development of a Scientific Permanent Scatterer System.* In: Proceedings Envisat Symposium 2004, Salzburg, September 6-10, ESA-SP572, p. 1-9 .

AMELUNG, F.; JONSON, S.; ZEBKER, H.A.; SEGALL, P. 2000. Widespread uplift and "trapdoor" faulting on Galápagos volcanoes observed with radar interferometry. **Nature**, v. 407, p. 993– 996.

BERARDINO, P.; FORNARO, G.; LANARI, R.; SANSOSTI, E. 2002. A new algorithm for surface deformation monitoring based on small baseline differential interferograms, **IEEE Trans. Geosci. Remote Sensing**, v. 40, p. 2375–2383.

CASU, F.; MANZO, M.; LANARI, R. 2006. A quantitative assessment of the SBAS algorithm performance for surface deformation retrieval from DInSAR data, **Remote Sensing of Environment**, v. 102, Issue 3-4, p. 195-210.

CHINI, M.; ATZORI, S.; TRASATTI, E.; BIGNAMI, C.; KYRIAKOPOLOUS, C.; TOLOMEI, C.; STRAMONDO, S. 2010. The May 12, 2008, (Mw 7.9) Sichuan earthquake (China): Multiframe ALOS-PALSAR DInSAR analysis of coseismic deformation, **IEEE Transactions on Geoscience and Remote Sensing Letters**, v.7, n. 2, p. 266–270.

COLESANTI, C.; FERRETTI, A.; NOVALI, F., PRATI, C., ROCCA, F. 2003. Monitoring of Progressive and Seasonal Ground Deformation. **IEEE Transactions on Geoscience and Remote Sensing**, v. 41, n. 7, p. 1685-1701.

CROSETTO, M.; CRISPA, B.; BIESCAS, E.; MONSERRAT, O.; AGUDO, M.; FERNANDES, P.; 2005. Land Deformation Monitoring Using SAR Interferometry: state-of-the-art. **Photogrammetr fernerkundung geoinformation**, v. 6, p. 497-510.

DAITO, K.; FERRETTI, A.; KUZUOKA, S.; NOVALI, F.; PANZERI, P.; ROCCA, F. 2003. L-band PS analysis: JERS-1 results and TerraSAR-L predictions, Proc. International Workshop on ERS SAR Interferometry (FRINGE03), Frascati, Italy, p1-6.

DEHLS, J. 2006. Permanent scatterer InSAR processing: Forsmark, Swedish Nuclear Fuel and Waste Management Co., SKB Rapport R-06-56, Stockholm Sweden, 34 ps.

ESA (EUROPEAN SPACE AGENCY) 2007. InSAR Principles: Guidelines for SAR Interferometry, Processing and Interpretation. ESA Publications ESTEC (TM-19), Noordwijk, The Netherlands, 40 ps.

FERNANDEZ, J.; TIZANNI, P.; MANZO, M., BORGIA, A.; GONZALEZ, P. J.; MARTI, J.; PEPE A.; CAMACHO A. G.;CASU, F.; BERARDINO, P.; PRIETO, J.F.; LANARI R. 2009. Gravity-driven deformation of Tenerife measured by InSAR time series analysis, **Geophysical Research Letters**, v. 36, p. L04306.

FERRETTI, A. 1999. Permanent scatterers in SAR interferometry, Proc. International Geoscience Remote Sensing Symposium., Hamburg, Germany, p.1528-1530.

FERRETTI, A.; PRATI, C.; ROCCA, F.; 2000. Nonlinear Subsidence Rate Estimation Unsing Permanent Scatterers in Differential SAR Interferometry. **IEEE Transactions on Geoscience and Remote Sensing**, v. 38, n. 5, p. 2202-2212.

FERRETTI A.; PRATI, C.; ROCCA, F. 2001. Permanent Scatterers in SAR Interferometry, **IEEE Transactions on Geoscience and Remote Sensing,** v. 39, n. 1, p. 8-20.

FERRETTI, A.; FUMAGALLI, A.; NOVALI, F.; PRATI, C.; ROCCA, F.; RUCCI, A. 2011. A New Algorithm for Processing Interferometric Data-Stacks: SqueeSAR. **IEEE Transactions on Geoscience and Remote Sensing**, v. 49, issue 9, p. 3460-3470.

GABRIEL, A. K.; GOLDSTEIN, R. M.; ZEBKER, H.A. 1989. Mapping small elevation changes over large areas: Differential radar interferometry. **Journal of Geophysical Research**, vol. 94. n. B7, p. 9183–9191.

GOLDSTEIN, R. M.; ENGELHARDT, R.; KAMP, B.; FROLICH, R. M. 1993.Satellite radar interferometry for monitoring ice sheet motion: Application to an Antarctic ice stream. **Science**, v. 262, p. : 1525–1530.

GRAHAM, L. C. 1974. Synthetic Interferometer Radar for Topographic Mapping. **Proceedings of the IEEE**, v. 62, n. 6, p. 763–768.

HANSSEN, R. F. 2001. **Radar Interferometry: Data Interpretation and Error Analisys Technique.** Kluwer Academic Publishers, Dordrecht. 328 ps

HASHIMOTO, M.; ENOMOTO, M.; FUKUSHIMA, Y. 2009. Coseismic deformation from the 2008 Wenchuan, China, earthquake derived from ALOS/PALSAR images, **Tectonophysics**, DOI: 10.1016/j.tecto.2009.08.034.

KAMPES, BERT M. 2006. **Radar Interferometry: Persistent Scatterer Technique.** Springer. 211 ps

LANARI, R.; LUNDGREN, P.; MANZO, M.; CASU, F. 2004. Satellite radar interferometry time series analysis of surface deformation for Los Angeles, California, **Geophysical Research Letter**, v. 31, n. 23, p. L23- 613.

LIVINGSTONE, C. E.; BRISCO, B.; BROWN, R. 1999. "On Being the Right Size": A Tutorial on Spatial Resolution in SAR Remote Sensing, Canada Centre for Remote Sensing, Internal Report, Ottawa, Canada, p. 35.

LOWMAN JR.; P. D.; HARRIS; J.; MASUOKA; P.M.; SINGHROY; V. H.; SLANEY, V. R. 1987. Shuttle Imaging Radar (SIR-B) Investigations of the Canadian Shield: Initial Report. **IEEE Transactions on Geoscience and Remote Sensing,** v. GE-25, n. 1, p. 55-66.

LU, Z.; KWOUN, O.; RYKHUS, R. 2007. Interferometric Synthetic Aperture Radar (InSAR): Its Past, Present and Future. **Photogrammetric Engineering & Remote Sensing**, v. March, p. 217-221.

MACDONALD 1979. Historical sketch: Radar Geology. in: Radar Geology: An Assessment, Report of the Radar Geology Workshop, Colorado, USA, p. 23-37 (JPL Publication 80-61).

MASSONNETT, D.; ROSSI, M.; CARMONA, C.; ADAGNA, F.; PELTZER, G., FEIGL, K.; RABAUTE, T. 1993. The displacement field of the Landers earthquake mapped by radar interferometry. **Nature**, v. 364, n. 8, p.: 138–142.

MASSONNETT, D.; BRIOLE, P.; ARNAUD, A. 1995. Deflation of Mount Etna monitored by spaceborne radar interferometry. **Nature**, V.375, p. 567–570.

MASSONNETT, D.; FEIGL, K. L. 1998. Radar interferometry and its application to changes in the earth's surface. **Reviews of Geophysics**, V. 36, n. 4: p. 441–500.

MIYAGI, Y.; OZAWA, T.; SHIMADA, M. 2009. Crustal deformation associated with an M8.1 earthquake in the Solomon Islands, detected by ALOS/PALSAR. **Earth and Planetary Science Letters**, p. 385-391.

MOORE, R. K.; CHASTANT, L. J.; PORCELLO, L. J.; STEVENSON, J.; ULABY, F. T. 1975. Microwave Remote Sensors, in: Manual of Remote Sensing, v. 1, chapter 9, Am. Soc. for Photog. and R.S, USA, p. 399-537.

MORA, O.; LANARI, R.; MALLORQUI, J. J.; BERARDINO, P.; SANSOSTI E. 2002. A new algorithm for monitoring localized deformation phenomena based on small baseline differential SAR interferograms. Proceedings IGARSS, Toronto, Canada, p. 1237-1239.

PEPE, A.; SANSOSTI, E.; BERARDINO P.; LANARI R. 2005. On the generation of ERS/ENVISAT DInSAR time-series via the SBAS technique, **IEEE Geoscience and Remote Sensing Letters**, v. 2, issue 3, p. 265-269.

PIGORINI, A.; RICCI, M.; SCIOTTI, A.; GIANNICO, C.; TAMBURINI, A. 2010. Satellite remote-sensing PSInSARTM technique applied to

design and construction of railway infrastructures. **Ingegneria Ferroviaria**, v. 9., p. 729-757.

RANEY, K. 1998. Radar Fundamentals: Technical Perspective, In: Manual of Remote Sensing, 3rd Ed., v. 2., chapter 2, Am. Soc. for Photog. and R.S., p. 9-130.

REALE, D.; NITTI, D. O.; PEDUTO, D.; NUTRICATO, F.; BOVENGA, F.; FORNARO, G. 2011. Postseismic deformation monitoring with the COSMO/SKYMED Constellation. **IEEE Geoscience and Remote Sensing Latters**, v. 8, n. 4, p. 696-700.

ROSEN A. R.; HENSLEY S.; JOUGHINMJ I. R.; LI F. K.; Madsen S. N.; Rodriguez E.; Goldstein R. M. 2000. Synthetic Aperture Radar Interferometry, **Proceedings of IEEE**, v. 88, n. 3, p. 333-382.

TRASATTI, E.; CASU, F.; GIUNCHI, C., PEPE, S., SOLARO, G.; TAGLIAVENTI, S.; BERARDINO, P.; MANZO, M.; PEPE, A.; RICCIARDI, G. P.; SANSOSTI, E.; TIZZANI, P.; ZENI, G.: LANARI, R. 2008. The 2004–2006 uplift episode at Campi Flegrei caldera (Italy): Constraints from SBAS-DInSAR ENVISAT data and Bayesian source Inference, **Geophysical Research Letters**, v. 35, p.L07308.

WEGMULLER, U.; VALTER, D.; SPRECKLS, V.; WERNER, C. 2010. Nonuniform Groung Motion Monitoring with TerraSAR-X Persistent Scatterer Interferometry. **IEEE Transactions on Geoscience and Remote Sensing**, v. 48, n. 2, p. 895-904.

WERLE, D. 1988. Radar Remote Sensing: A Training Manual. Dendron Resources Survey, Canada Centre for Remote Sensing, Ottawa, Canada, 213 ps.

WILEY, C. 1954. Pulsed Doppler Radar Method and Means, US Patent No. 3.196.436.

ZEBKER, H. A.; GOLDSTEIN, R. M. 1986. Topographic mapping from interferometric synthetic aperture radar observations. **Journal of Geophysical Research**, v. 91(B5), p. 4993–4999.

ZEBKER, H. A.; VILLASENOR, J. 1992. Decorrelation in interferometric radar echoes. **IEEE Transactions on Geoscience and Remote Sensing**, v. 30, n. 5, p. 950-959.